# Inert atmosphere processing of hydroxyapatite in the presence of lithium iron phosphate

Miodrag J. Lukić,*[1] Maja Kuzmanović,[1] Meltem Sezen,[2] Feray Bakan,[2] Adela Egelja,[3] Ljiljana Veselinović[1]

[1]Institute of Technical Sciences of the Serbian Academy of Sciences and Arts, Belgrade, Serbia

[2]Sabanci University Nanotechnology and Application Center (SUNUM), Istanbul, Turkey

[3]Vinca Institute of Nuclear Sciences, University of Belgrade, Belgrade, Serbia

*corresponding author: miodrag.lukic@itn.sanu.ac.rs

## Abstract

The present study describes sintering behaviour of hydroxyapatite (HAp) upon addition of lithium iron phosphate (LFP) (1-10 wt. %) system in inert (Ar) atmosphere. The interaction between materials and melting of LFP influenced early and intermediate stages of HAp sintering, shifting the densification curves towards low-temperature side. Analysis of densification process indicated significant differences upon LFP addition. The reaction mechanism that assumes the initial interaction between phosphates from LFP and calcium from HAp was proposed, generating calcium vacancies and contributing to HAp densification. Cross-sections of sintered samples showed changes in microstructural properties, with uniform atomic distribution and presence of $Li_2Fe_3O_4$ spherical inclusions (200 nm) located at grain boundaries of calcium phosphate matrix. The Rietveld refinement analysis indicated changes in structural and microstructural parameters like crystallite size, anisotropy and microstructural strain of HAp upon LFP addition. Mechanical characterisation indicated improvements in fracture behaviour upon LFP addition.

*Keywords*: hydroxyapatite, sintering, phase transformation, microstructure

## 1. Introduction

Materials based on hydroxyapatite (HAp) ceramics are widely studied as components for medical applications, sensors, magnetic separations, catalyst support, etc[1–4]. Different engineering and scientific approaches, like microstructural optimization [5–8] and addition of different additives [9,10], were implemented for enhancement of functional response. Numerous alkali-based compounds were investigated as useful additives for inducing liquid phase formation during HAp sintering [11]. The addition of Li to HAp [12], as well as the presence of $Li_3PO_4$ in air atmosphere [13], was reported to enhance sintering behaviour by an improved atomic diffusion and eutectic formation. Li addition was found to be useful for microstructural and mechanical properties improvement and for increase of electrical conductivity [12]. On the other side, there are no enough reliable data on the mechanism by which Fe-compounds influence HAp sinterability. The addition of Fe to HAp was considered from the point of view of imparted magnetic response [9,14]; furthermore, formation of metallic, especially Ti-Fe inclusions, in a brittle ceramic matrix was found to be useful for fracture resistance improvement [15]. Generally, achieving a certain level of multifunctionality within HAp-based bioceramics for specific purposes could make a progress in applications of HAp-based materials. Lithium iron phosphate (LFP) is interesting as a sintering aid for HAp, since it melts around 960 - 1000 °C in inert atmosphere [16], which is usually in the intermediate stage of HAp sintering regardless its stoichiometry or synthesis method [17–19]. Exploitation of these findings accompanied with an appropriate sintering cycle, could induce changes in the HAp sintering behaviour through the formation of liquid phase. Furthermore, the understanding of underlying sintering mechanism and phase evolution can provide a basis for further development of multifunctional calcium phosphate system.

To the authors' best knowledge, this is the first study focusing on sintering behaviour of HAp–LFP system. An in-depth characterization was performed, giving the full insight into synthesized materials properties, thermal behaviour, densification, chemical and microstructural features.

## 2. Materials and methods

HAp powder was synthesized by aqueous chemical precipitation. Ca/P ratio of precursors was set to stoichiometric 1.67. $Ca(NO_3)_2 \cdot 4H_2O$ (Fluka, Germany) was used as a source of $Ca^{2+}$ ions, whilst $PO_4^{3-}$ ions were obtained from 85 % orthophosphoric acid, $H_3PO_4$ (Lach-Ner, Czech Republic), with density of 1.7 $gcm^{-3}$. 25 % $NH_4OH$ (Superlab, Serbia) was used as a precipitating agent. 50 g of $Ca(NO_3)_2 \cdot 4H_2O$ was dissolved in 300 ml of distilled water, whilst the phosphate solution was made by dissolving of 8.60 ml of 85 % $H_3PO_4$ in the same amount of water. pH values of precursor solutions were adjusted to 11 prior to reactants mixing. Phosphate solution was dropwise added to calcium solution at room temperature, and the resulting mixture was boiled and naturally cooled down to room temperature. The precipitate was aged for 24 h in a native solution and washed out to pH 7. The obtained filter cake was dried at 80 °C for 18 h and crushed in an agate mortar. LFP was prepared by a hydrothermal method, starting from aqueous solutions of $LiOH \cdot H_2O$ (Centrohem, Serbia), $FeSO_4 \cdot 7H_2O$ (Fluka, Germany), $(NH_4)_2HPO_4$ (Fluka, Germany) and citric acid, $C_6H_8O_7$ (Alkaloid, FYR Macedonia) in a molar ratio of 3:1:1:1, respectively. $FeSO_4$ and $C_6H_8O_7$ were dissolved in distilled water, and afterwards, LiOH solution was added, with constant stirring. Finally, an aqueous solution of $(NH_4)_2HPO_4$ was intermixed. The suspension was transferred to a stainless steel Teflon-lined hydrothermal reactor with the inner volume of 75 ml. Overall solution volume was 45 ml. The concentration of $Fe^{2+}$ ions was 0.3 M, and pH of the final suspension was 6. The hydrothermal reactor was heated to 180 °C and kept for 7 hours. After hydrothermal treatment, the reaction mixture was cooled down to room temperature. Precipitate was separated from the solution by centrifugation. After separation, the slurry was washed out with distilled water and dried at 80 °C for 24 hours. Synthesized materials were mixed in an aqueous suspension under effective stirring for 3 h at room temperature and dried for 18 h at 80 °C in the final step.

X-ray powder diffraction (XRD) measurements were used to identify crystal phases in the synthesized powders. The data were collected on a Philips PW 1050 X-ray powder diffractometer using Ni-filtered $CuK\alpha_{1,2}$ (40 kV, 20 mA) radiation and Bragg–Brentano focusing geometry. Measurements

were done at room temperature over $2\theta$ range of 15–60 ° with 0.05 ° scanning step width and counting time of 3 s per step. The detailed structural and microstructural analysis was done by Rietveld refinement procedure for HAp and HAp + 5 % LFP samples after non-isothermal sintering. The data for Rietveld analysis were recorded from 10 to 100 ° $2\theta$, using step size of 0.02 ° and counting time of 12 s per step. The structural refinements were performed using the *FullProf* computer program in *WinPLOTR* environment [20],[21–23]. The Rietveld refinements started from the fixed unit-cell parameters calculated by LSUCRI [24] and atomic positions reported in the literature [25]. The Thompson–Cox–Hastings (TCH) pseudoVoigt (pV) profile function was used to describe peak profiles. The background description was performed by a 6-coefficient polynomial function.

The effective broadening models, as well as TCH-pV profile functions implemented in the Rietveld method and *FullProf* computer program, allow studying of microstructural effects [23,26–28]. The crystallite size anisotropy was simulated using spherical harmonics, while strain anisotropy effects were described based on a quartic form model [27]. In order to exclude instrumental broadening, the XRD pattern of a $LaB_6$ standard was fitted. The obtained resolution function ($U$ = 0.000761817, $V$ = -0.000546506, $W$ = 0.00268110, $X$ = 0.0570382, $Y$ = 0.0217545) were calculated in the microstructural analysis.

Specific surface area of HAp powder was determined to be 73 $m^2/g$, whilst that of LFP was only 1.06 $m^2/g$ (Supporting info). The carbonate content in the HAp powder was determined by the elemental analysis, and was found to be 1.5 wt. % (Supporting info). Particle size distribution (PSD) was recorded with Malvern Mastersizer 2000 device, using aqueous suspensions of 5 mg powder in 10 ml distilled water, after 3 min of sonication in an ultrasonic bath. The obtained data were extracted as volume (V) and number (N) fractions. Thermomechanical analysis (TMA) was done on a vertical dilatometer system (Setsys Evolution, Setaram, France) with an alumina flattened probe and contact loading of 5 g in Ar atmosphere up to 1200 °C. Heating rate was 10 °$Cmin^{-1}$ whilst cooling down to room temperature was naturally with the furnace. Green pellets were prepared by uniaxially pressing of powders in 6 mm ∅ molds, with 500 kg load. The height of samples, $h$, was recorded and compared with the initial height, $h_o$. Simultaneous thermal analysis was performed (Setsys Evolution, Setaram,

France) in platinum (100 µl) crucibles, in Ar atmosphere. Before introducing Ar atmosphere, working environment was evacuated up to $10^{-2}$ mBar pressure and purged with 200 $mlmin^{-1}$ flow rate of Ar for 30 min. Ar was introduced into a furnace at 20 $mlmin^{-1}$ flow rate during both heating and cooling regime. Mass spectra were recorded on a quadrupole mass spectrometer (Pfeiffer, Germany) with an acquisition time of 200 ms/amu, for *m/z* values of 7, 17, 18 and 44, assuming single electron ionization. Fourier transform infrared (FTIR) spectra of the samples were recorded at ambient conditions in the mid-IR region (400-4000 $cm^{-1}$) with a Nicolet IS 50 FT-IR spectrometer operating in ATR mode and measuring resolution of 4 $cm^{-1}$ with 32 scans. All spectra were normalized to the phosphate vibration mode at 604 $cm^{-1}$. Microstructural characterization of sintered ceramics was done by scanning electron microscopy (SEM) using a JEOL 4601F MultiBeam Platform with FEG-SEM, equipped with an energy dispersive spectrometer (EDS-Xmax N SDD Oxford Instruments, Great Britain). An electron probe at low acceleration voltages (3-5 kV) was applied. Using a dual-beam platform, the samples were cross-sectioned at 30 keV and moderate ion ($Ga^+$) currents, and EDS maps and related spectra were acquired on the sections. Therefore the elemental distribution inside the material was revealed. The signal from Ga was excluded from presented EDS spectra since it originates from ion-milling. The micro-mechanical testing by Vickers indentation with 500 g load and 15 s dwell time (Buehler, model Micromet 5101) was performed to give an indication of development of mechanical properties upon non-isothermal sintering of HAp with LFP addition. All data are collected for at least 5 indentations. The values of hardness are taken from provided tables according to the indent diagonal lengths, whilst fracture toughness, $K_{IC}$, is calculated per Evans-Charles formula, considering the applied load and length of propagated cracks [29].

## 3. Results

### 3.1. Physico-chemical characterization of powders

Fig. 1a shows XRD patterns of synthesized HAp and LFP powders. All reflections are assigned to pure HAp (P63/*m*, hexagonal crystal structure, ICSD 99358) and LFP (P*nma*, orthorhombic crystal structure, ICSD 97764) materials. HAp crystallite size in [002] crystallographic direction is 8.1 nm,

while the crystallinity degree of HAp was estimated to 26 %, according to the method described previously [30]. Crystallite size of LFP in [311] crystallographic direction is determined to be 37 nm. Summarized values of crystallite size, unit cell parameters (*a*, *b*, *c*) and unit cell volume (*V*), as well as the average particle size, are presented in Table SI (Supporting Info). Volume and number PSDs of HAp, Fig. 1b, reveal peaks 6 μm and 400 nm, respectively, while those of LFP, Fig. 1c, are around 10 μm and 250 nm, respectively.

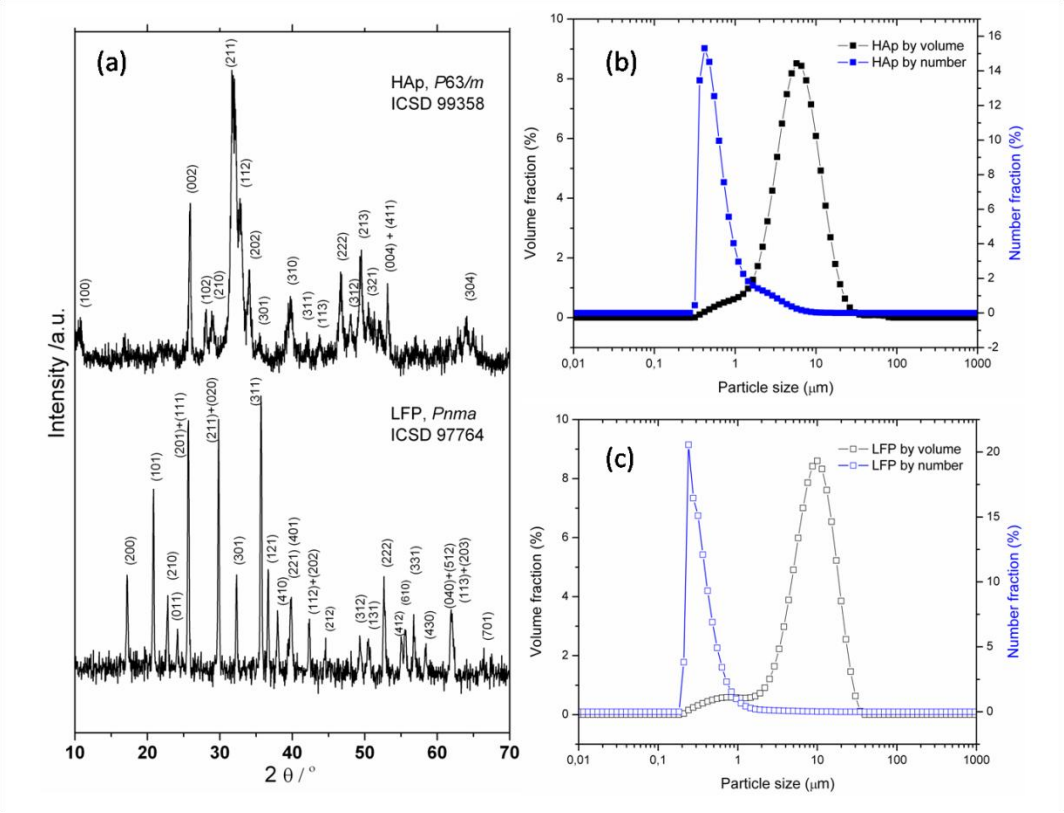


Fig. 1. (a) XRD patterns and PSDs of (b) HAp and (c) LFP powders. (2-column fitting image)

SEM images showing morphology and particle size of selected powders are shown in Fig. 2. HAp is consisted of spherical particles, Fig. 2a, with a diameter of 50 nm, slightly agglomerated into the submicrometer clusters. On the other side, LFP powder is consisted of rectangular, highly-agglomerated particles of few hundred nanometers.

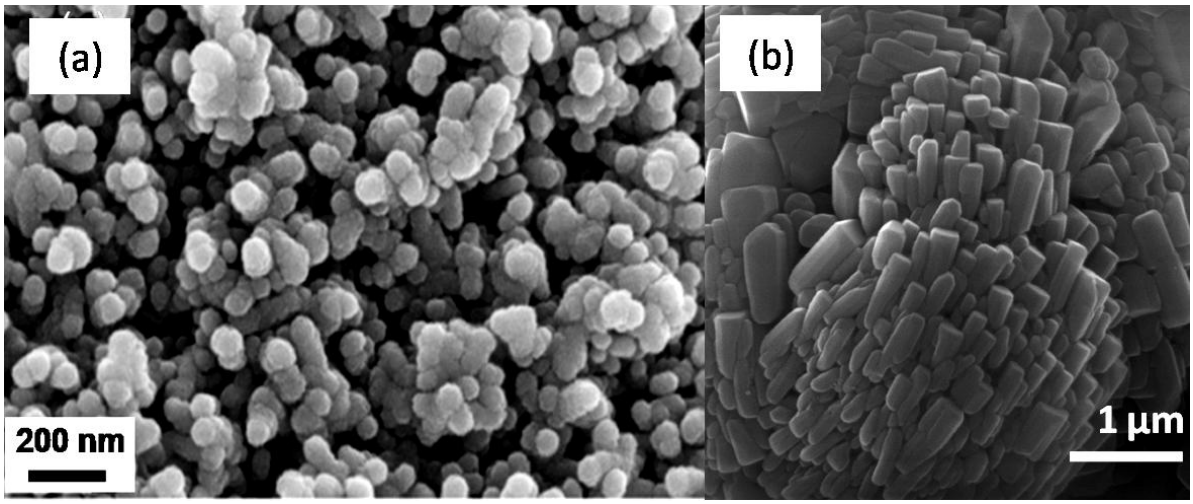


Fig. 2. SEM images of (a) HAp and (b) LFP powders (2-column fitting image)

FTIR spectrum of HAp powder is shown in Fig. 3. It can be seen that vibration modes of phosphate, hydroxyl and carbonate functional groups are present, along with some traces of surface bound water. The observed phosphate vibration modes are: ν1 symmetric stretching mode at 961 $cm^{-1}$, triple degenerative asymmetric stretching mode ν3 between 1000 and 1150 $cm^{-1}$, double degenerative bending ν4 mode at 564 and 603 $cm^{-1}$, as well as double degenerative ν2 mode at 471 $cm^{-1}$. Vibrations of hydroxyl group can be observed at 632 and 3568 $cm^{-1}$. The presence of surface bound water is detected as broad features around 1650 and 3430 $cm^{-1}$, without any traces of nitrate or ammonium residuals in FTIR spectrum. Vibration modes of carbonates incorporated in HAp crystal structure can be observed at 874 (ν2) and at 1420 and 1456 $cm^{-1}$ (ν3), corresponding to B-type carbonated HAp (substitution at the place of $PO_4$ group). Having this in mind, the synthesized HAp can be considered as B-type carbonated HAp.

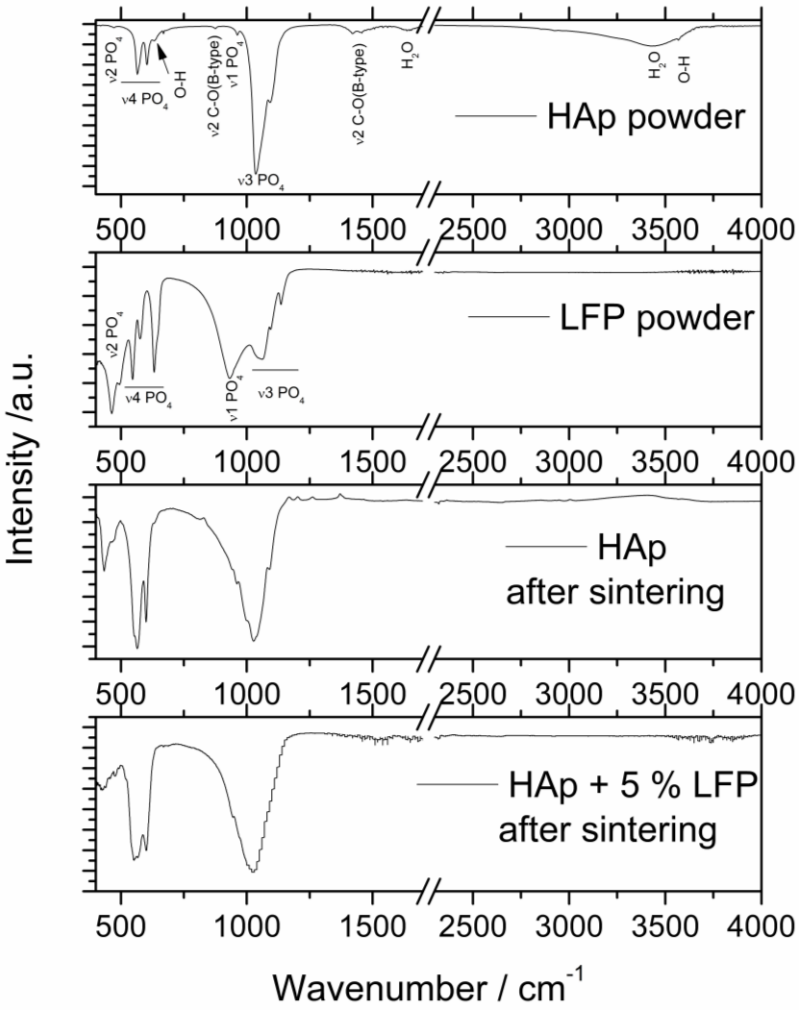


Fig. 3. FTIR spectra of HAp and LFP powders, and HAp and HAp + 5 % LFP samples after non-isothermal sintering. (single column fitting image)

Vibration spectrum of LFP shows fundamental $PO_4^{3-}$ modes ν1-ν4, split in several components due to interaction with Fe-O units in the crystal structure [31]. The vibration modes of phosphates are observed at 933 $cm^{-1}$ (slightly shifted asymmetric stretching mode, ν1), doublet ν2 from 461 to 495 $cm^{-1}$, triplet ν3 from 1057 to 1137 $cm^{-1}$ and triplet ν4 from 544 to 631 $cm^{-1}$. The vibration modes of phosphate group certainly exist in both HAp and LFP compounds, indicating the existence of the common chemical functionality.

3.2. Thermal analysis

Thermal analysis of LFP in air atmosphere was performed to investigate thermal stability under oxidative environment and to determine the amount of carbon retained after synthesis, Fig. 4a. LFP undergoes a thermal oxidation process accompanied with mass increase and corresponding exothermic peaks in DTA plot around 325 and 590 °C. According to the previously described procedure, the amount of remained atomic carbon is determined from the difference between mass gain due to $Fe^{2+}$ oxidation (theoretically 5.07 % for pure LFP), and mass gain of investigated material [32], indicating that 2.9 wt. % of carbon remained in the LFP powder.

Any indication of LFP melting in air atmosphere up to 1000 °C is not observed. Corresponding mass spectrum, Fig. 3b, reveals peaks that originate from $CO_2$ release, having the most intensive features between 200 and 450 °C, and after 750 °C. A slight Li sublimation current can be observed at temperatures between 250 and 310 °C, while remaining water is almost continually released during heating.

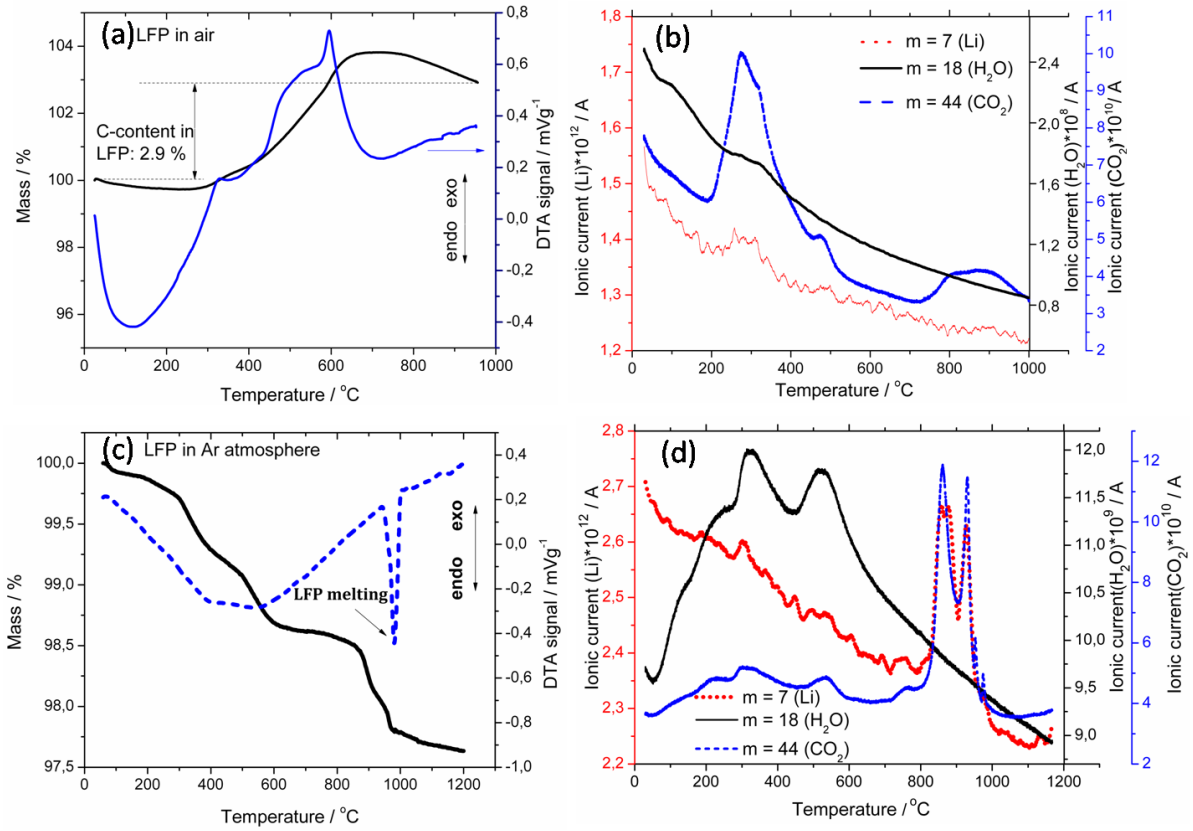

Fig. 4. TG-DTA and mass spectra of prepared LFP in air, (a) and (b), and in inert (Ar) atmosphere, (c) and (d). (2-column fitting image)

Processing of LFP in Ar atmosphere induced completely different thermal response, Fig. 4c. Mass of material decreased in several steps, with final mass loss around 2.4 wt. %. DTA plot shows an intensive sharp endothermic peak between 950 and 1000 °C corresponding to LFP melting, without any traces of oxidative behaviour. Mass spectrometry analysis, Fig. 4d, indicates that mass decrease in the regions up to 600 °C can be ascribed to water loss with the most intensive peaks at 325 and 525 °C, whilst $CO_2$ and Li releases are detected in two steps preceding the melting region, around 860 and 930 °C. Considering the level of mass change in the region of Li sublimation and $CO_2$ release, which is below 1 wt. %, no significant compositional and physicochemical changes are expected that can influence further behaviour.

Having described the thermal behaviour of LFP in oxidative and inert atmospheres, the basis for further investigation of thermal behaviour of HAp–LFP system is provided. Thermal analysis of pure HAp in Ar atmosphere up to 1200 °C, Fig. 5a, with corresponding mass spectrometry, Fig. 5b, shows a continual mass loss characteristic for HAp. At lower temperatures, loosely bound water molecules release the material, while at higher temperatures, structural dehydroxylation process takes place. Evaporation of water molecules during heating is almost continual with temperature and reaches a plateau at 900 °C. Carbonates leave material at specific temperature ranges: ~ 300, 550 – 625, and 930 °C. The final mass loss is around 8 wt. %. DTA plot shows several endothermic peaks: around 100 °C due to water release, and around 625 and 930 °C due to carbonates evaporation. The endothermic shoulder around 850 °C probably originates from slight phase transformation of HAp to β-TCP, since the thermal processing in inert atmosphere favours dehydroxylation and decrease of structural stability.

Influence of LFP addition on thermal behaviour was demonstrated on sample with 5 wt. % of LFP. TG/DTA plot, Fig. 5c, of HAp + 5 % LFP sample is similar to the results obtained for HAp: characteristic DTA signals of water release (~100 °C) and endothermic trend around 600 °C are

observed. Broad endothermic feature between 750 - 875 °C indicates earlier phase transformation while that at 980 °C shows the trace of LFP melting. Carbonates evaporation peaks, Fig. 5d, are found around 250, 500 and 600 °C, whilst the most intensive one is at 875 °C.

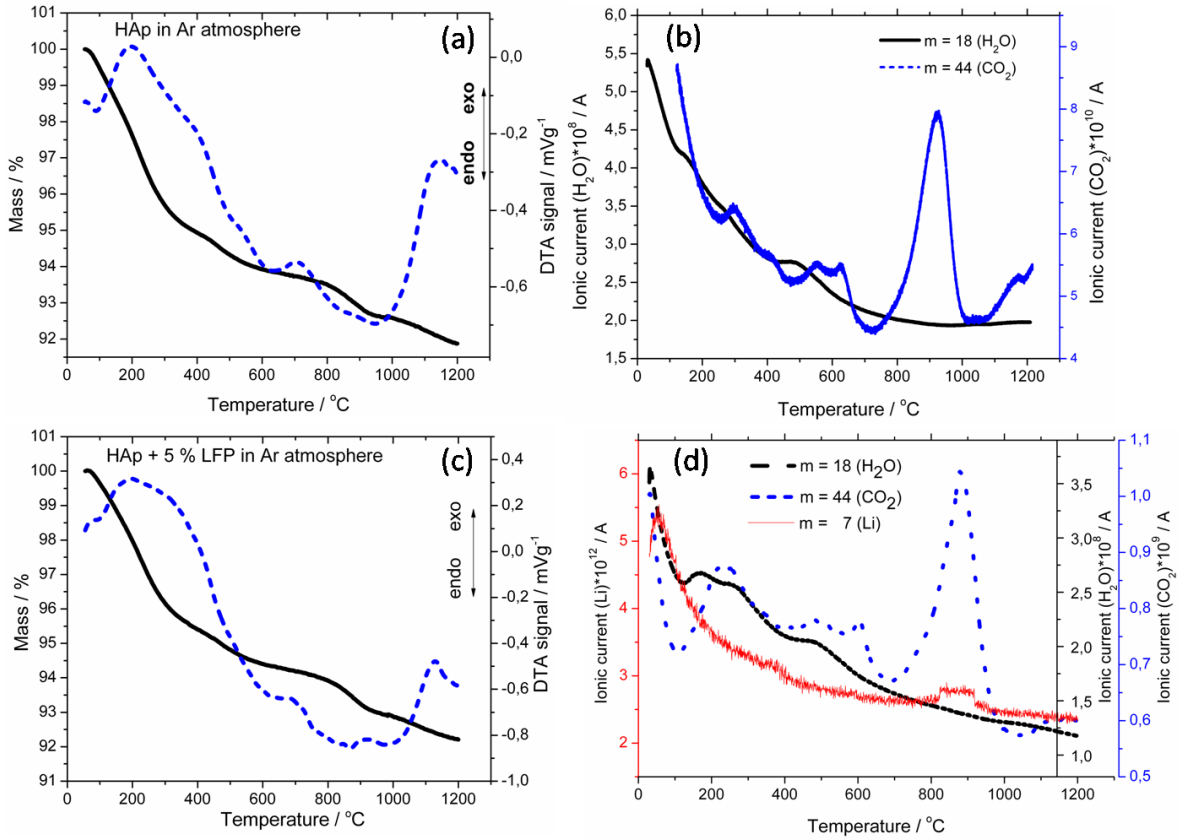


Fig. 5. TG-DTA and mass spectra of HAp, (a) and (b), and HAp + 5 % LFP, (c) and (d), in inert (Ar) atmosphere. (2-column fitting image)

3.3. Non-isothermal sintering behaviour

Densification and densification rate plots during non-isothermal sintering of HAp with the different amounts of added LFP are shown in Fig. 6. It is observed that HAp exhibits poor densification behaviour (Fig. 6a), without reaching the final sintering stage plateau. The addition of LFP induced shifting of densification curves towards lower temperatures. The temperature of densification onset is gradually decreased with increasing LFP content in the green samples. In the intermediate sintering stage, samples with 1 and 2 wt. % of LFP retain characteristic sigmoid shape of densification curve

whilst sample with 5 wt. % of LFP clearly shows the change in slope, indicating different sintering mechanism. This trend is confirmed for sample with 10 wt. %. of LFP, however, a certain dilatation process appears around 1150 °C.

Quantitatively, the values of absolute density of HAp and HAP + 5 % LFP samples are 1.96 and 2.43 g/cm$^3$ at 1000 °C, respectively, whilst at 1100 °C, these values are 2.30 and 2.68 g/cm$^3$, respectively. At the highest investigated temperature (1200 °C), absolute densities of all samples are similar, between 2.70 and 2.90 g/cm$^3$; however, the densification pathways are completely different.

The analysis of influence of LFP addition on densification rate is given in Fig. 6b. HAp sample clearly exhibits two separate densification regions, represented with the sharp peak at 980 °C, and broad feature between 1000 and 1150 °C. The addition of LFP influences the position of the former peak, shifting it to the low-temperature side, while the later appears as a satellite feature which gradually loses its intensity. The sample with 5 wt. % of LFP shows the most uniform peak of densification rate near 920 °C, with a minimal contribution of high-temperature shoulder. The trend continues for sample with 10 wt. % of LFP.

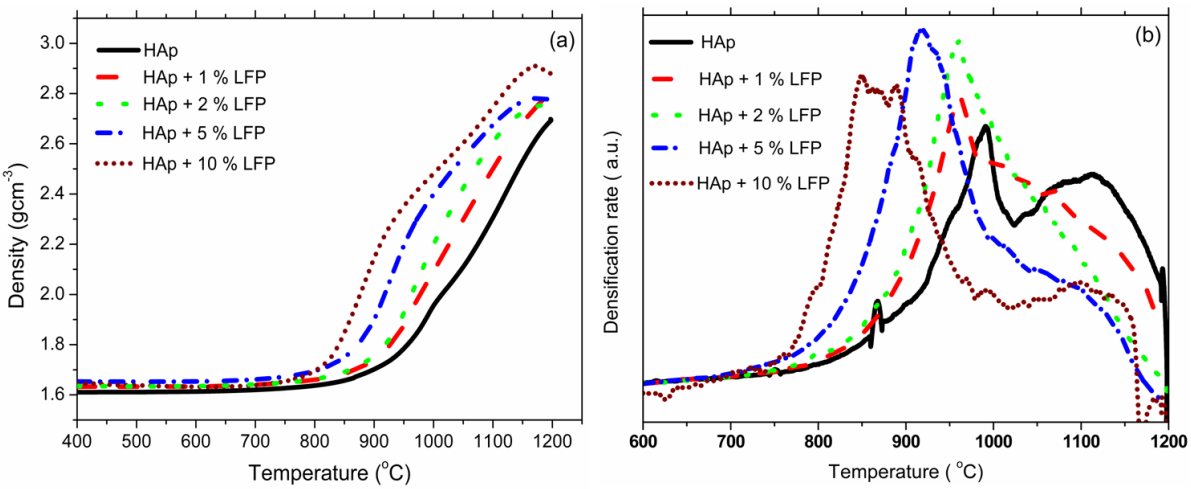


Fig. 6. (a) Non-isothermal densification and (b) densification rate of HAp with different amount of LFP up to 1200 °C in inert (Ar) atmosphere. (2-column fitting image)

The analysis of mass spectra recorded during non-isothermal sintering of pure HAp, Fig. 6a, and HAp + 5 wt. % LFP, Fig. 6b, shows a continual water loss with exponentially decreasing intensity. Furthermore, an exchanged profile of carbonates evolution from crystal lattice at higher temperatures can be observed, whilst it is almost the same at low-temperature side. Presence of LFP provokes earlier release of incorporated carbonates: for pure HAp ceramics, it is peaked around 925 °C, whilst for the HAp + 5 wt. % LFP sample is at 875 °C, which agrees with the findings of thermal analysis. Generally, a broad feature of carbonates loss is shifted for 50 degrees towards lower temperatures for sample containing LFP. For both samples, the maxima of carbonates release peaks correspond to the temperature of shrinkage values of 2-3 %. Considering Li release for HAp + 5 wt. % LFP sample, a slight increase in ionic current is detected, overlapping release of carbonates above 800 °C.

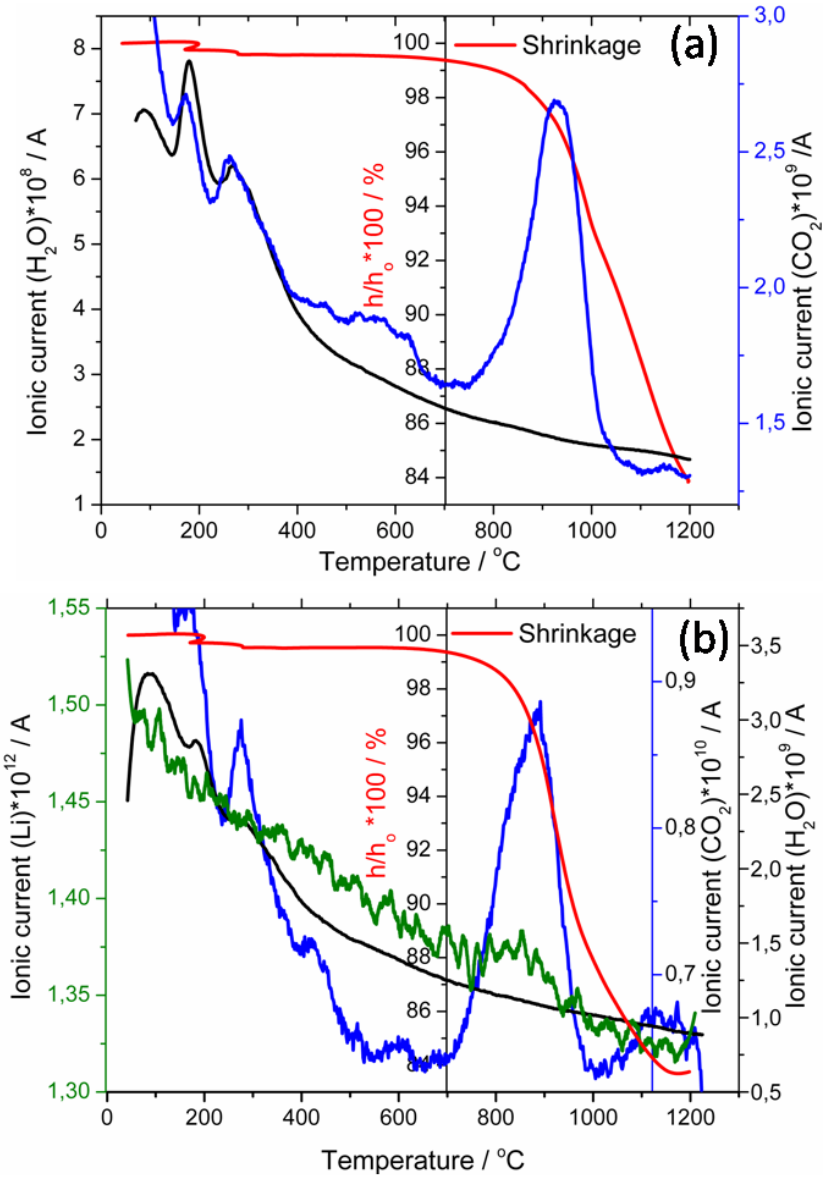


Fig. 7. Shrinkage curves with corresponding mass spectra of (a) HAp and (b) HAp +5 % LFP in inert (Ar) atmosphere. (single column fitting image)

3.4. Microstructural, chemical and phase analysis

Microstructural properties of polished and thermally etched samples after non-isothermal sintering are shown in Fig. 8. It can be seen that different microstructural features are present depending on the amount of initially added LFP. HAp sample after non-isothermal sintering consists of a conventional microstructure, with the existence of elongated pores and rather broad grain size distribution due to the uncontrolled grain growth. The average grain size is approximately around 500 nm. The addition

of 1 % of LFP resulted in microstructure larger grains. The trend of grain growth with LFP addition was also confirmed for HAp + 5 % LFP sample. However, this sample clearly exhibits the presence of two different kinds of microstructural features: a fraction of larger grains, with grain size on a micrometer level, and smaller grains, nearly 200-300 nm in size, located along the grain boundaries of the larger grains. Also, a certain amount of closed, round pores can be found at grain junctions. Contrary to the aforementioned samples, microstructure of HAp + 10 % LFP was quite different. Besides the largest grains among the investigated samples, it can be observed that grains have rounded edges and that pores are larger and more spherical in shape which can originate from formation of higher amount of liquid phase during the processing stage. The appearance of larger pores is in agreement with the observation of dilatation in densification curve at 1160 °C.

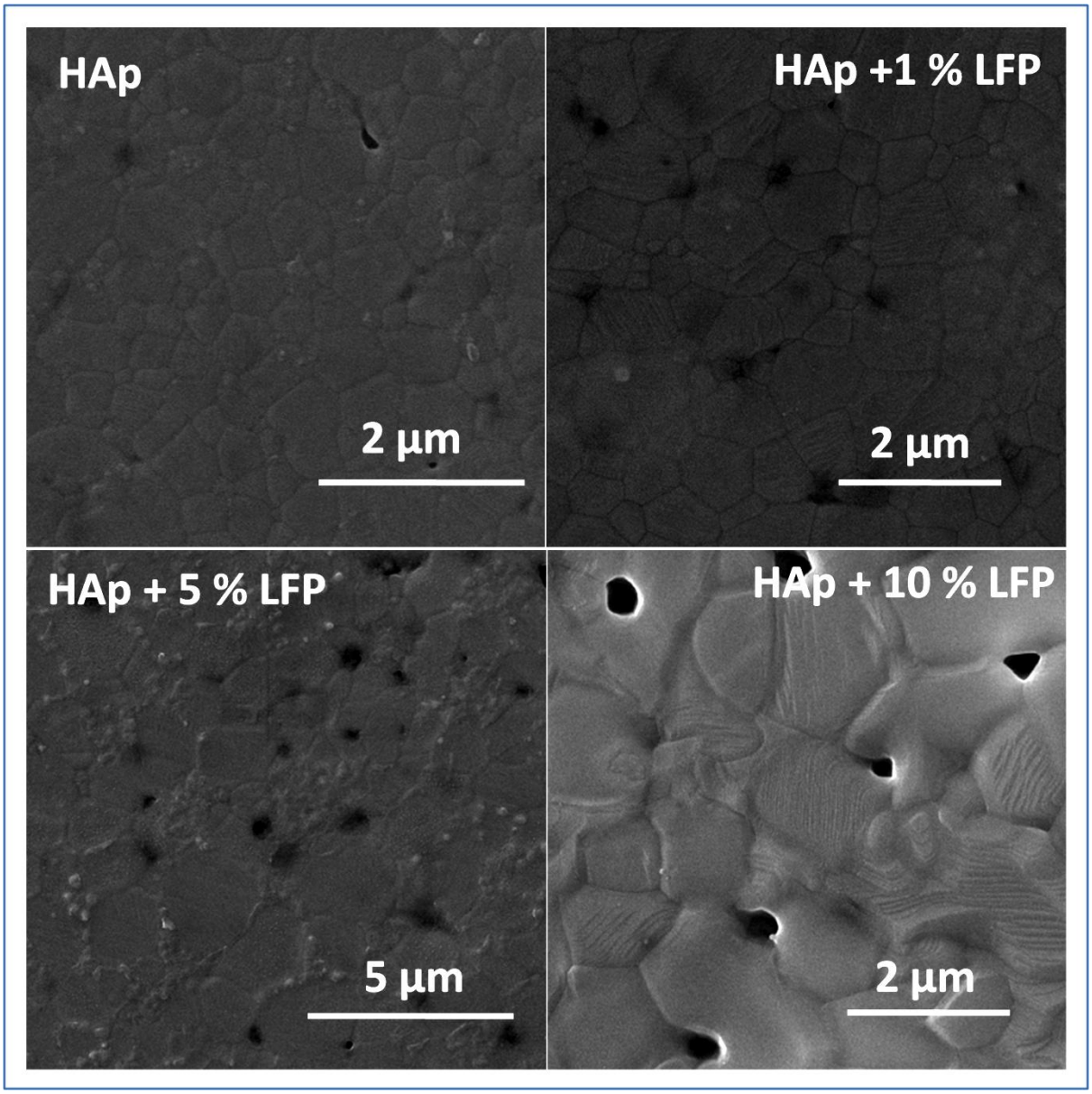


Fig. 8. SEM micrographs of microstructural profile of non-isothermally sintered ceramics with different amount of added LFP. (2-column fitting image)

Microstructural profile is revealed by cutting the sample with low-intensity focused ion ($Ga^{+}$) beam. During the milling stage, it is observed that behaviour of samples against ion-milling was changed: HAp tends to be milled in a vertical direction, whilst it is more horizontal with LFP addition (HAp + 5 % LFP).

Several microstructural regions of sintered HAp + 5 % LFP sample were chosen for EDS analysis: different places (10 spots) in the laminar region and flat surface (Fig. 9a) as well as specific microstructural features observed in the flattened region (Fig. 9b). It can be seen that both laminar and flat regions are consisted of main atomic constituents of calcium phosphate ceramic phases, Ca, P, O, as well as a trace from Fe, Fig. 9c. Also, low amount of C remained in the material after decomposition of organic phase is also detected. However, EDS analysis of uniformly distributed spherical inclusions with a size between 150 and 250 nm, Fig. 9d, reveals an intensive Fe peak besides those from Ca, P and O. Elemental mapping of flattened area (Fig. 9a) indicated the existence of homogeneous atomic distribution within the material with the presence of specific Fe-rich spherical inclusions (Fig. 9b). The measured atomic composition of characteristic microstructural regions is given in Table I.

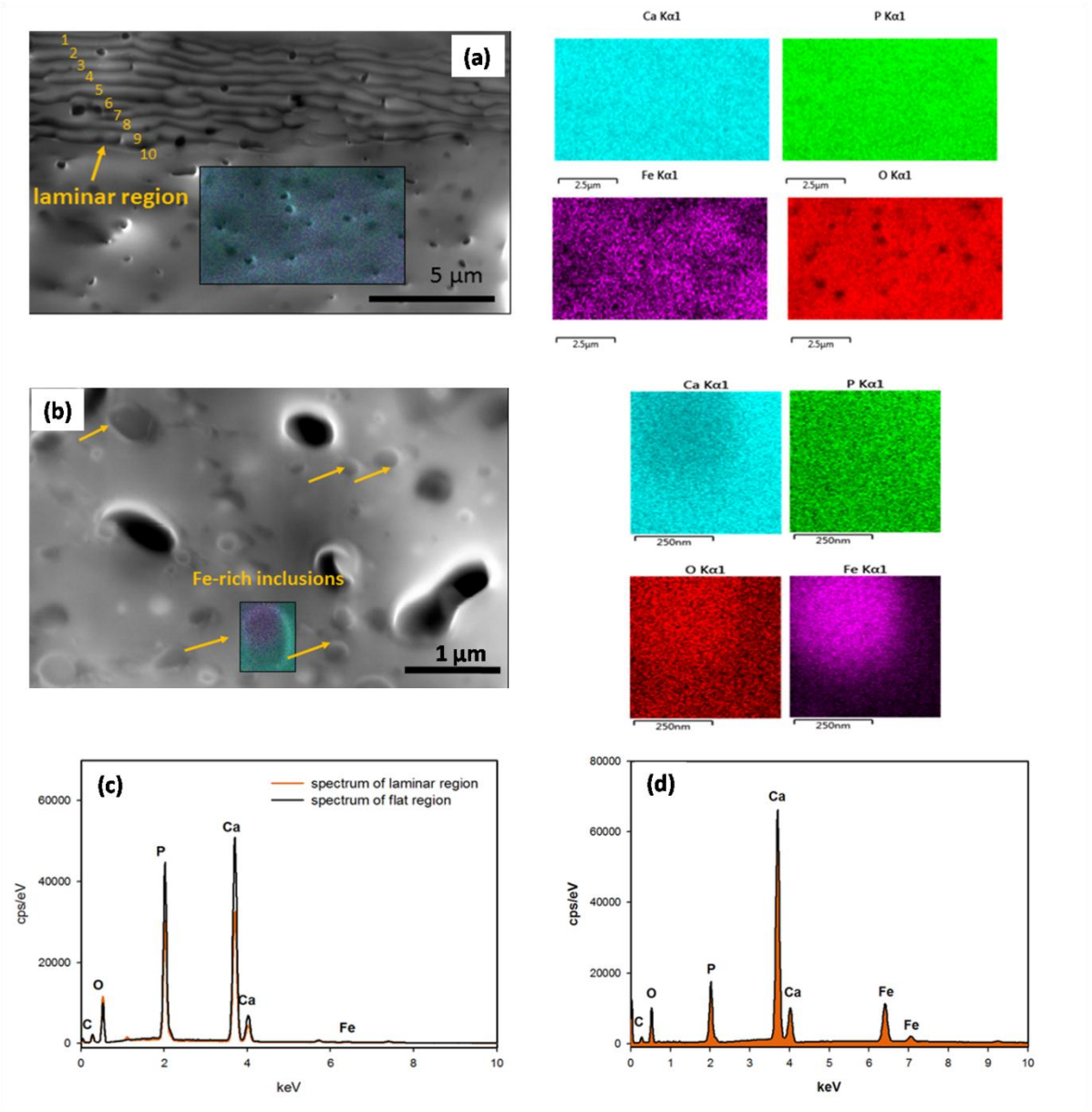


Fig. 9. (a) SEM micrograph of laminar and flat regions of HAp +5 % LFP sample with elemental distribution; (b) SEM micrograph of magnified flat region with clearly observable spherical inclusions with elemental mapping showing Fe-rich region; EDS spectra of (c) laminar and flat regions and (d) Fe-rich inclusions. (2-column fitting image)

Table I. Atomic composition of characteristic microstructural regions.

| Element | Flat region / % wt. | Laminar region / % wt. | Fe-rich inclusions/ % wt. |
|---|---|---|---|
| Ca | 41.4 | 43.1 | 53.5 |
| P | 20.8 | 22.4 | 6.0 |
| O | 36.8 | 33.5 | 7.1 |
| Fe | <1.0 | <0.9 | 33.3 |

FTIR spectra of non-isothermally sintered HAp and HAp + 5 % LFP samples are shown in Fig. 3. HAp shows characteristic vibrations of $PO_4^{3-}$ group: ν1 vibration at 961 $cm^{-1}$, ν2 mode at 474 $cm^{-1}$, ν3 between 1000 and 1150 $cm^{-1}$ with peaks at 1044 and 1091 $cm^{-1}$, and ν4 mode at 568 and 602 $cm^{-1}$. Vibrations of O-H group are presented as low-intensity peak around 3560 $cm^{-1}$. In the case of HAp + 5 % LFP sample, complex ν3, as well as ν4, phosphate mode is represented by the broader peak, without clear vibration near 1090 $cm^{-1}$. Moreover, peaks of ν1 and ν3 vibrations are shifted towards lower energies. ν4 vibration mode at 565 $cm^{-1}$ shows splitting and formation of two modes at 551 and 570 $cm^{-1}$. Vibration modes of carbonates incorporated in HAp crystal lattice can be observed neither for HAp nor for HAp + 5 % LFP, except some surface bound $CO_2$ and $H_2O$ in HAp + 5 % LFP, probably upon handling.

XRD patterns, Fig. 10, show final phase compositions of the non-isothermally sintered ceramics. Sintering in inert atmosphere up to 1200 °C contributes to slight thermal instability of HAp itself and resulted in a dominant presence of HAp phase with small amount of α-TCP phase in the material. Here should be noted that heating of the powder and/or prolonged sintering in air atmosphere did not result in any TCP phase formation (Fig. S1, Supporting info). TCP formation in Ar atmosphere was favoured by shifting chemical equilibrium of dehydroxylation reaction. The addition of LFP changed the phase composition of sintered materials. Instead of high-temperature TCP phase, in the case of HAp +1 % LFP, besides HAp, the main phase is low-temperature rhombohedral β-TCP. When initial

amount of LFP is increased to 2 wt. %, the same phases are present; however, the amount of β-TCP phase is higher than in the previous sample and the same trend continues with the addition of 5 % of LFP. For sample with added 10 wt. % of LFP, β-TCP is dominant phase, with small amounts of non-transformed HAp in the final ceramics. Moreover, in the case of samples with higher LFP amounts, reflections at 36.7 and 42.7 *2θ* degrees in the XRD patterns appear, and thus the surrounding regions are magnified to reveal the nature of crystallized phase. According to the previously reported data, the reflections can be assigned to $Li_2Fe_3O_4$ compound that forms under inert atmosphere conditions, without $Fe^{2+}$ oxidation [33,34]. Summarized phase composition of sintered samples is given in Table SII (Supplementary info).

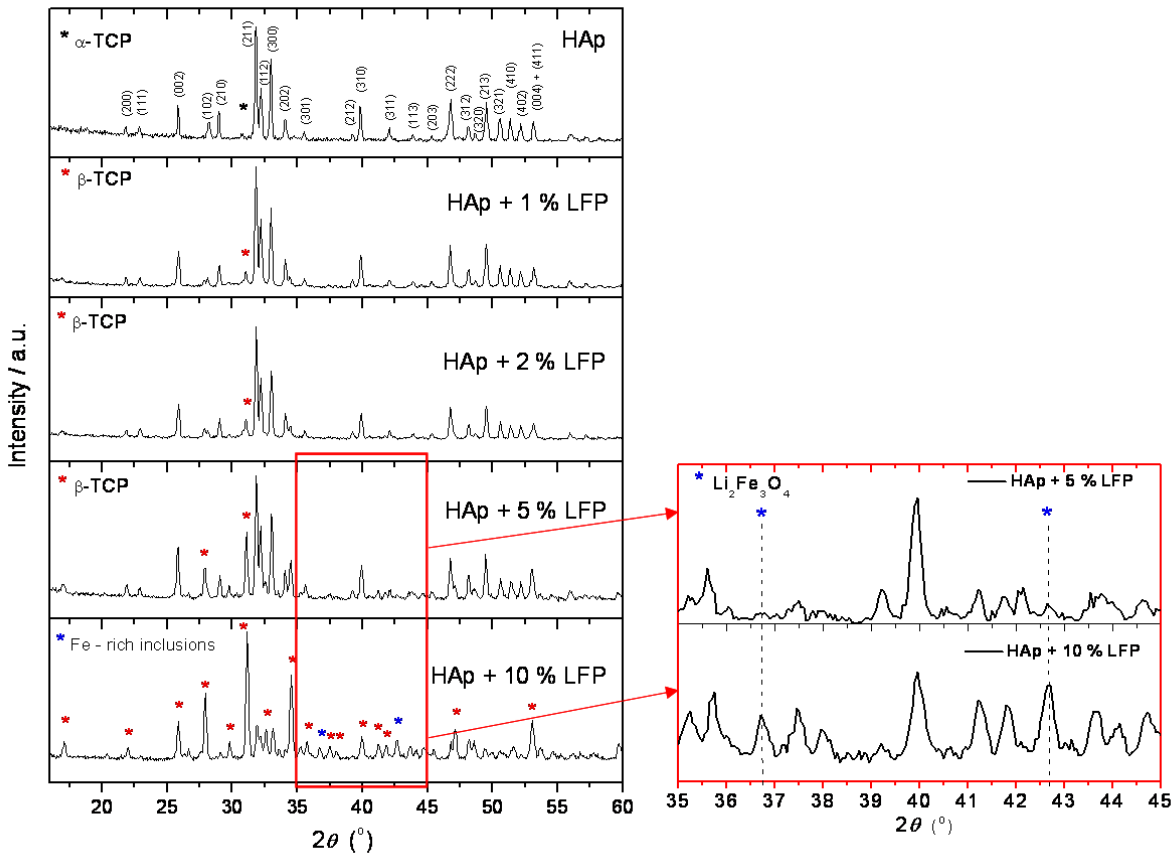


Fig. 10. XRD patterns of non-isothermally sintered ceramics up to 1200 °C. (single column fitting image)

### 3.5 Rietveld refinement

Rietveld refinement procedure was conducted using the *FullProf* computer program to identify any structural and microstructural changes in HAp crystal lattice parameters due to the potential incorporation of foreign ions in HAp crystal lattice. Since the amount of added LFP is small and that HAp + 10 % LFP sample after sintering showed the dominant presence of β-TCP, the procedure was performed only for HAp and HAp + 5 % LFP sample. The atomic positions and space group ($P6_3/m$, SG 176) of HAp were used as a starting set in the refinement procedure for both powders [25]. The structural refinement procedure confirmed that the materials after non-isothermal sintering are consisted of two phases. The best agreement between observed and calculated powder patterns for processed HAp sample was achieved when refined as the mixture of HAp ($P6_3/m$) and $\alpha$-TCP ($P2_1/a$) (Fig. 11a), while the best compliance for HAp + 5 wt. % of LFP sample was obtained when the refinement was carried out as a mixture of HAp ($P6_3/m$) and $\beta$-TCP ($R3c$). The obtained values of the agreement factors (HAp: Rp = 6.87, Rwp = 9.35; HAp + 5 % LFP: Rp = 6.55, Rwp = 8.60) confirmed the validity of applied structural models (Table SIII, Supporting info).

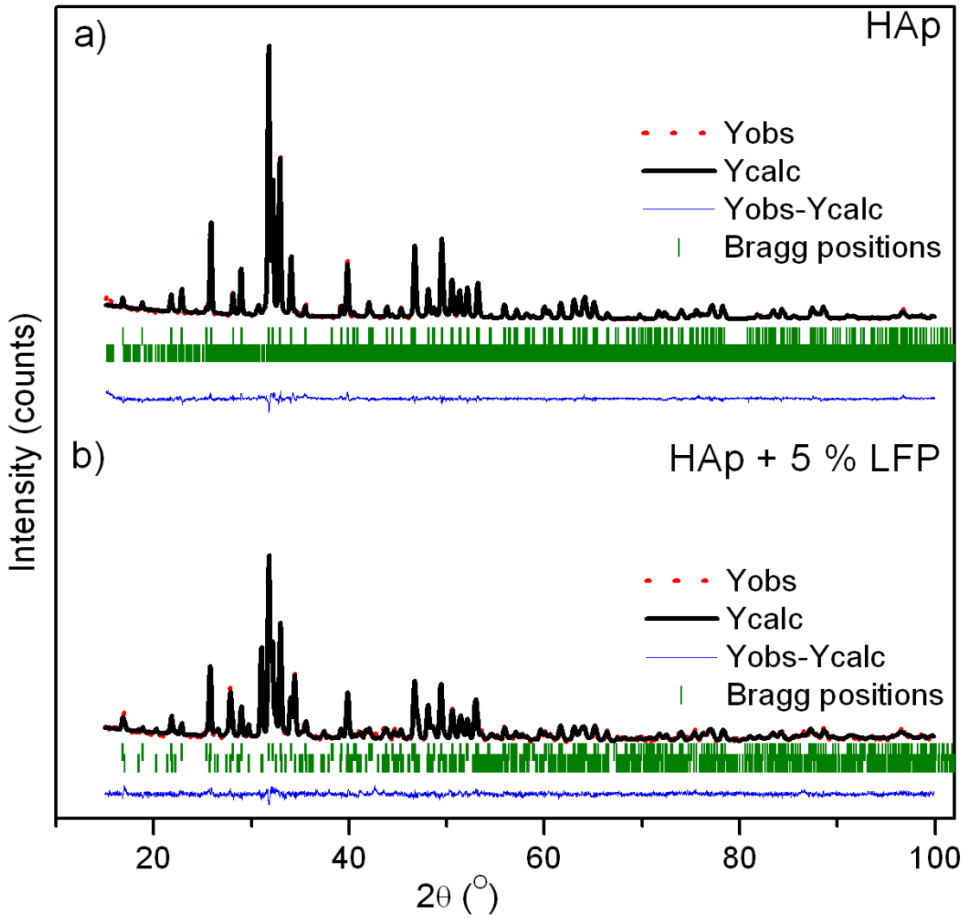


Fig. 11. Final Rietveld refined plots of (a) HAp and (b) HAp + 5 % LFP samples after non-isothermal sintering. (single column fitting image)

The refined unit-cell parameters and cell volumes are presented in Table II. The addition of LFP provokes decreasing of HAp unit cell parameters: $a = b$ decreases from 9.4171(5) to 9.4089(7) Å, while $c$ decreases from 6.8851(3) to 6.8671(4) Å, yielding the decrease in unit cell volume. This can be a consequence of incorporation of smaller ions in the crystal structure of HAp. This was corroborated by calculation of average bond distances values, Table III: calculated average Ca1–O bond length value decreases from 2.564 (HAp) to 2.558 Å (HAp + 5 % LFP) and Ca2–O from 2.457 (HAp) to 2.444 Å (HAp + 5 % LFP ).

Table II. The refined values of unit-cell parameters and cell volume.

| Samples | Phases | Unit cell parameters | | | |
|---|---|---|---|---|---|
| | | a (Å) | b (Å) | c (Å) | V (Å$^3$) |
| Hap | HAp ($P6_3/m$) (~ 93 %) | 9.4171(5) | | 6.8851(3) | 528.75(4) |
| | $\alpha$-TCP ($P2_1/a$) (~ 7%) $\beta$=126.25(3) | 12.975(6) | 26.874(1) | 15.238(6) | 4284.92(3) |
| HAp + 5 % LFP | HAp ($P6_3/m$) (~ 80 %) | 9.4089(7) | | 6.8671(4) | 527.36(3) |
| | $\beta$-TCP ($R3c$) (~ 20 %) | 10.4126(14) | | 37.4399(2) | 3515.49(6) |

Table III. The agreement factors, structural and microstructural parameters after non-isothermal sintering.

| | Ca1 | Ca2 | P | O1 | O2 | O3 | O4 |
|---|---|---|---|---|---|---|---|
| HAp | | *Rp*= 6.87 | *Rwp*= 9.35 | | | | |
| *x* | ⅔ | 0.2449(5) | 0.3681(7) | 0.4834(9) | 0.4606(5) | 0.2569(7) | 0 |
| *y* | ⅓ | -0.0082(6) | 0.3977(8) | 0.3278(3) | 0.5796(6) | 0.3416(2) | 0 |
| *z* | 0.0012(1) | ¼ | ¼ | ¼ | ¼ | 0.0695(1) | 0.1866(3) |
| *B*(Å$^2$) | 2.82(2) | 3.03(1) | 3.02(2) | 2.87(2) | 2.87(2) | 2.87(2) | 2.87(2) |
| Occ | ⅓ | ½ | ½ | ½ | ½ | 1 | 0.1666 |
| Average distances (Å) Ca1—O =2.564 Ca2—O=2.457 | | | | | | | |
| Average crystallite size (nm) *D*=53 | | | | | | | |
| Average strain 29.24x10$^4$ | | | | | | | |
| HAp + 5% LFP | | *Rp* = 6.55 | *Rwp*= 8.60 | | | | |
| *x* | ⅔ | 0.2452(2) | 0.3991(1) | 0.3277(2) | 0.5873(1) | 0.3414(3) | 0 |
| *y* | ⅓ | 0.9931(2) | 0.3681(1) | 0.4821(4) | 0.4660(4) | 0.2596(2) | 0 |
| *z* | 0.0025(3) | ¼ | ¼ | ¼ | ¼ | 0.0676(2) | 0.1845(3) |
| *B*(Å$^2$) | 2.49(3) | 2.71(1) | 3.00(2) | 2.04(2) | 2.04(2) | 2.04(2) | 2.04(2) |
| Occ | ⅓ | ½ | ½ | ½ | ½ | 1 | 0.1666 |
| Average distances (Å) Ca1—O =2.558 Ca2—O=2.444 | | | | | | | |
| Average crystallite size (nm) *D*=34 | | | | | | | |
| Average strain 34.43x10$^4$ | | | | | | | |

Furthermore, it is obvious that LFP in HAp sample causes decreasing and broadening of diffraction maximum intensity, which indicates lower crystallinity, smaller values of crystallite size and higher microstrain values (Fig. 11). The influence of added LFP on the microstructural properties (size and strain) of HAp was determined by analysis of broadening and shape of diffraction maxima using the Rietveld method and *FullProf* computer program. The visualizations of crystallite shape anisotropy as well as microstrain anisotropy are shown in Fig. 12. It can be seen that the presence of LFP in HAp sample provokes decreasing of average crystallite size from 53 to 34 nm (Table III) as well as reduction of the crystallite size anisotropy (Fig. 12a). On the other side, the presence of LFP caused increasing of microstrain value from $29.24 \cdot 10^4$ to $34.34 \cdot 10^4$ (Table III) and appearance of the microstrain anisotropy (Fig. 12b).

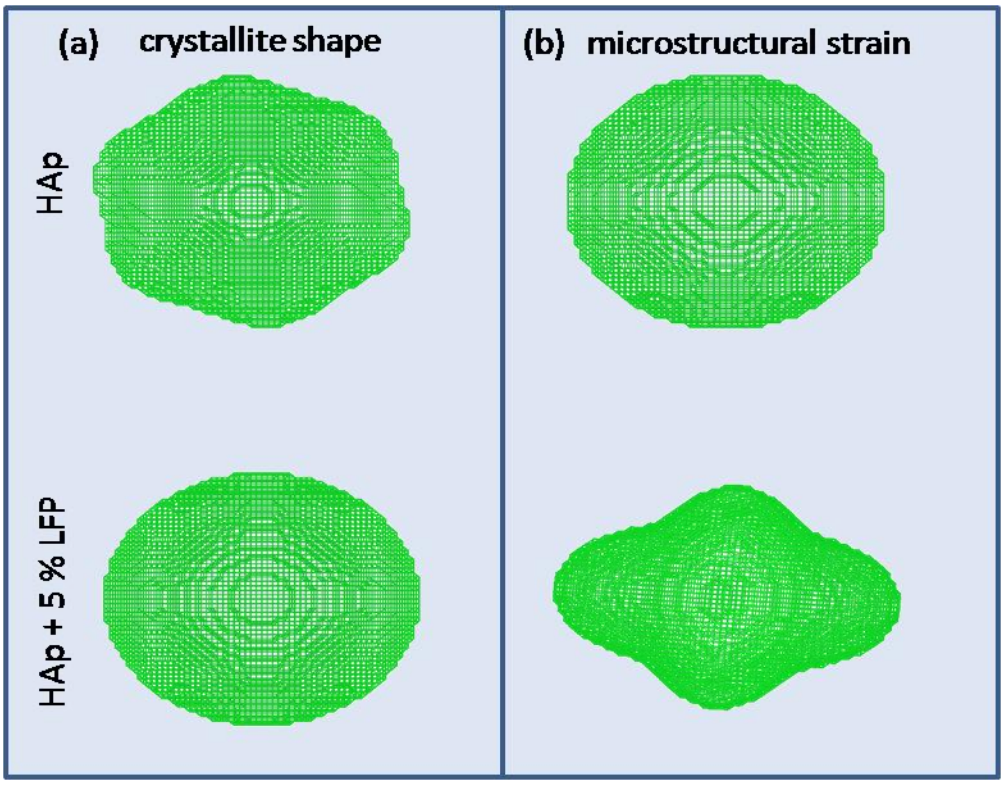


Fig. 12. (a) Crystallite shape and (b) microstructural strain of HAp and HAp + 5 % LFP samples after non-isothermal sintering. (2-column fitting image)

### 3.6. Mechanical measurements

According to the already reported literature, the addition of Li or Fe can contribute to improved electrical and mechanical properties of HAp. The mechanical measurements showed that hardness is not significantly changed and almost stayed in the area of standard deviation or is lower for samples with added LFP, which can be a consequence of liquid phase formation during sintering and microstructural softening. However, fracture toughness of sintered ceramics increased with added LFP, especially for HAp + 5 % LFP and HAp + 10 % LFP samples, indicating the beneficial effect. This can originate from formation of identified $Li_2Fe_3O_4$ microstructural features located along the grain boundaries of matrix phase, which act as mechanical energy-dissipating agents that suppress crack propagation.

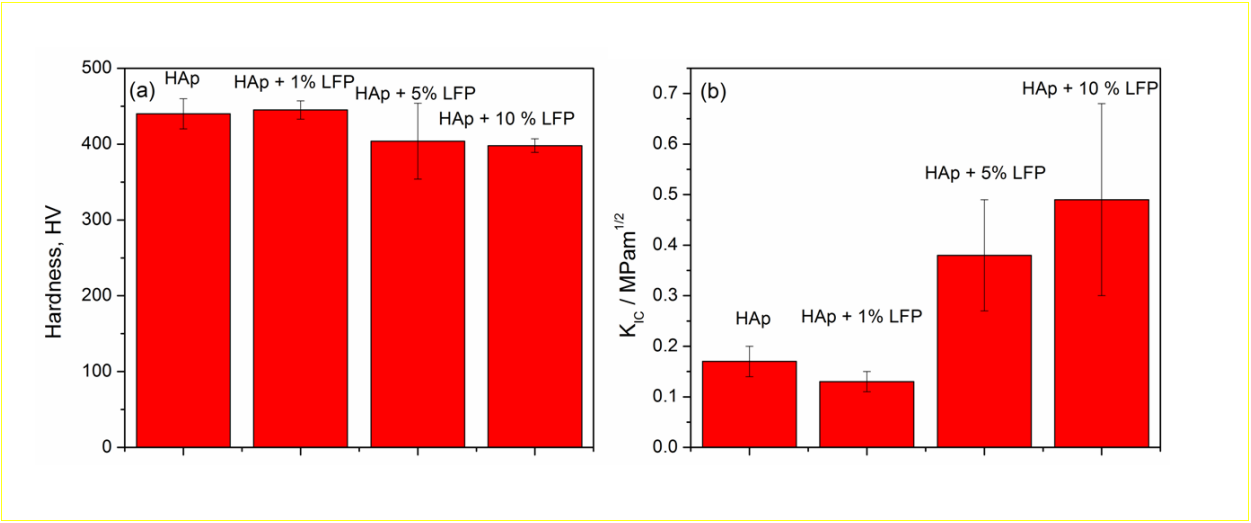


Fig. 13. (a) Vickers hardness and (b) fracture toughness properties of final ceramics upon non-isothermal sintering (2-column fitting image).

The low values of obtained fracture toughness for all samples can be understood from the point of final density, since materials are not fully densified; however, it gives a clear indication of the favourable mechanical response upon the LFP addition.

## 4. Discussion

Since the investigated materials have very distinct area of applications, previous studies have not reported results on sintering behaviour of HAp–LFP system; however, considering HAp ceramics, addition of the different Li- or Fe-compounds were proved to be an efficient method for enhancing densification, mechanical and electrical properties [12,13,35]. Moreover, HAp and LFP possess tetrahedral phosphate group as a common functionality which makes these systems interesting for further investigation.

Chemical precipitation method has been showed as a practical and useful approach for synthesis of nanocrystalline HAp ceramics [36]. Unit cell parameters as well as specific surface area of the prepared HAp were of the expected size when compared to biological HAp [37] with a certain amount of incorporated carbonates, having the similar apparent particle size as LFP powder. Moreover, specific surface area of LFP could is very low, which implies that improvement in sintering behaviour cannot be ascribed to the effects of additional surface development.

Working atmosphere for thermal processing of this system arose as one of the most influential parameters. Processing in air atmosphere resulted in expected oxidation of LFP [32]. However, processing in inert (Ar) atmosphere showed stable system up to almost 950 °C, where intensive melting occurred. These experimental observations implied that further studies of the influence of LFP on sintering behaviour of HAp ceramics require inert atmosphere processing. HAp showed similar thermal behaviour in inert atmosphere as that exhibited in air [38], with a certain level of thermal instability being promoted by the absence of moisture in inert conditions and enhanced dehydroxylation [39]. The addition of LFP to the matrix material induced important differences in thermal behaviour comparing to pure HAp ceramics. Low-temperature carbonate release peak (~ 600 °C) can be ascribed to small amount of A-type carbonates, whilst that at higher temperatures should be from B-type carbonates in HAp crystal lattice [40]. Endothermic peak around 830 °C of HAp + 5 % LFP sample implies that LFP favours phase transformation and low-temperature TCP phase

formation. This foregoing interaction between two materials probably provoked the release of carbonates from HAp crystal lattice at lower temperatures, particularly at 870 °C.

Non-isothermal sintering behaviour of HAp materials with different amount of added LFP showed improved densification in the intermediate sintering stage, earlier onset of sintering and overall shifting of densification curves towards lower temperatures. Enhancing the densification in low-temperature range with LFP addition could imply the change towards mass transport mechanisms that involve atomic flux from grain boundary and/or volume regions. In the light of identified $Li_2Fe_3O_4$ inclusions, the reaction mechanism that involves interaction between Ca from HAp and $PO_4$ group from LFP is proposed. Since the phosphate group is a common chemical functionality of HAp and and that there is no phosphate group in the final Li-Fe compound described above, it is reasonable to assume that chemical reaction between HAp and LFP starts via the phosphate groups of LFP. From the side of HAp, the chemical reaction at high temperatures starts from Ca ions, and tricalcium phosphate, β-TCP, $Ca_3(PO_4)_2$, is formed. This reaction pathway can be supported also by the slight Ca over-stoichiometry (Ca/P > 1.67) due to B-type carbonation in the place of phosphates, $Ca_{10-x}(PO_4)_{6-x}(CO_3)_x(OH)_{2-x}$. In that way, when interaction started, the amount of Ca in HAp actually decreases, as well as the Ca/P ratio, in the presence of LFP, favouring further high-temperature HAp decomposition and formation β-TCP. This can explain why the amount of β-TCP phase in the final ceramics critically increased with LFP addition, being the dominating calcium phosphate phase of final ceramics after sintering for HAp + 10 % LFP initial composition. Moreover, along with reaction of phosphates from LFP and Ca from HAp and subsequent formation of Ca vacancies in HAp structure, a certain amount of $Fe^{2+}$ ions can incorporate in HAp crystal lattice, which explains the findings from the Rietveld. The phosphate-depleted LFP can tend to form the identified $Li_2Fe_3O_4$ compound, accompanied by slight Li sublimation observed experimentally. Although the quantitative mechanism cannot be exactly deduced herein, the chemical reaction taking place during inert atmosphere processing of HAp-LFP system can be represent as follows:

$Ca_{10-x}(PO_4)_{6-x}(CO_3)_x(OH)_{2-x} + LiFePO_4 \rightarrow Ca_{10-x}Fe_x(PO_4)_6(OH)_2 + Ca_3(PO_4)_2 + Li_2Fe_3O_4 + \uparrow CO_2 + \uparrow Li$

The subsequent partial reactions that take place are:

(i) $(Ca)_{HAp} - (PO_4)_{LFP} \rightarrow \beta\text{-}Ca_3(PO_4)_2$

(ii) Ca-deficient HAp – $(Fe)_{LFP} \rightarrow$ Fe-HAp – $\beta\text{-}Ca_3(PO_4)_2 - H_2O - \uparrow CO_2$

(iii) $PO_4$-deficient $LiFePO_4$ (condensation) $\rightarrow Li_2Fe_3O_4 - \uparrow Li$

The formation of Ca vacancies, due to the reaction between HAp and LFP, as additional mass transport pathways, contributes to densification of the HAp-LFP system. Furthermore, formation of β-TCP induces release of structural OH, which can additionally improve sintering of the materials. Such behaviour resulted that 10 % shrinkage of HAp + 5 % LFP sample occurs more than a hundred degrees earlier than for HAp sample. It was previously found that Li-compound addition favours liquid phase formation during sintering and reduced β-TCP content of sintered ceramics [41], whilst in the case of added of $Li_3PO_4$ phase, the eutectic point was found at 1010 °C [13]. Formation of liquid phase could be also assigned to this system, influencing changes in the shape of densification curves, decrease of their slope at corresponding temperatures (depending on LFP amount), and pore and grain boundary rounding. However, it should be noted that in the reported data, sintering atmosphere, as well as starting Li-compound, were different. In the case of HAp–LFP system, LFP addition stimulated β-TCP formation, stabilizing it even up to 1200 °C, which is higher than temperature of β→α-TCP phase transition. Nevertheless, the incorporated carbonates (1.51 wt. %) could influence densification process. In the case of pure HAp, such content of carbonates may induce lowering of densification around 950 °C to the certain extent, Fig. 6b; however, for samples with added LFP, especially higher amounts, the other processes probably overlap the effect of decarbonation and densification lowering should be considered from the point of exhausted reaction potential between HAp and LFP.

Considering the observed microstructural changes, the appearance of specific microstructural features with the addition of LFP phase could be correlated with melting and interaction of LFP with the matrix material. Different behaviour against ion-milling could give some clues regarding morphological organization or alignment of the inner-structure of the sintered materials. Formation of spherical $Li_2Fe_3O_4$ inclusions within calcium phosphate matrix revealed that places of inclusions are actually the initial positions of LFP particles/agglomerates. From these points started interaction with the matrix material and melting of LFP, initializing liquid phase sintering and phase transformation. Having in mind the results of microstructural investigations, it can be considered that uniformly distributed inclusions along grain boundaries of calcium phosphate matrix could be beneficial for enhancing mechanical properties since it was found that micrometer-sized Fe-Ti particles were useful for fracture toughness improvement [15].

The Rietveld refinement analysis showed that decrease in unit cell parameters as well as in length of Ca–O bonds in HAp crystal structure. This can occur due to the partial replacement of $Ca^{2+}$ by smaller ions. Having in mind that the theoretical sum of six-coordinated $Fe^{2+}$ and $O^{2-}$ ionic radii is 2.01 Å [42], previous findings that after non-isothermal sintering length of Ca1–O and Ca2–O bonds decreases from 2.564 (HAp) to 2.558 Å (HAp + 5 % LFP) and 2.457 (HAp) to 2.444 Å (HAp + 5 % LFP ), respectively, corroborate the ionic replacement of larger $Ca^{2+}$ ion (1.0 Å for sixfold coordination) by smaller $Fe^{2+}$ cation (0.61 Å in sixfold coordination) in HAp crystal structure. It was already reported that the partial replacement of Ca atoms in the HAp structure by ions with smaller ionic radius provokes a decrease in cell volume [43–45]. On the other hand, it is reported that incorporation of 3*d*-metal ions in a hexagonal channel of the apatite structure causes the expansion of the unit cell [46,47]. Herein, the contraction is observed for both *a* and *c* unit cell parameters. Song et al. reported that doping with 0.2 mol. % of $Fe^{2+}$ at pH 12 resulted in decrease of *a* and increase in value of *c* unit cell parameter, with indication that such replacement occurs at Ca1 position [48]. Furthermore, crystallinity was lowered [48]. In the case of $Fe^{3+}/Zn^{2+}$ co-doping of HAp, decrease in both *a* and *c* parameters was observed [49], while $Fe^{3+}$ doping was also attributed to decrease in crystallinity of HAp [50]. The findings of decreased crystallite anisotropy and crystallinity, and

increased microstructural strain of sample processed in the presence of LFP suggest that partial incorporation of $Fe^{2+}$ into HAp crystal lattice could occur. Having in mind that the amount of Li in the investigated system is very low, and that there are no adequate literature data on influence of Li incorporation on HAp crystal lattice parameters, the question of $Li^{+}$ incorporation in HAp crystal lattice herein is still illusive, although it is possible if the value of its ionic radius is considered.

## 5. Conclusions

HAp–LFP system was studied regarding thermal and sintering behaviour in inert atmosphere conditions. It was found that LFP interaction with the matrix material and its melting in intermediate sintering stage of HAp can be successfully exploited to enhance the sintering behaviour of matrix material. Densification process shifted towards lower temperatures with increase of LFP amount for almost 150 degrees, and change of sintering mechanism. The reaction mechanism that assumes initial reaction between phosphates from LFP and Ca from HAp was proposed, inducing formation of critical amount of TCP and slight Fe-incorporation in HAp. Moreover, the Rietveld refinement procedure showed that crystallite size, crystallinity and shape anisotropy of HAp decreased upon sintering due to LFP addition, whilst its microstructural strain value and anisotropy increased, indicating interactions at crystal lattice level. Specific $Li_2Fe_3O_4$ inclusions located at grain boundaries of calcium phosphate matrix were observed, and the favourable mechanical response of the sintered ceramics was indicated.

## Acknowledgements

These results were obtained through the collaboration of the Institute of Technical Sciences of the Serbian Academy of Sciences and Arts with Sabanci University Nanotechnology Research and Application Center (SUNUM) starter through JECS Trust funded training school. The authors would like to thank the Ministry of Education, Science and Technological Development of the Republic of Serbia under grant III 45004. Also, the authors are grateful to Dr. A. Mraković from Vinča Institute of

Nuclear Sciences, Serbia, for FTIR measurements, Dr. M. Maček-Kržmanc and Dr. S.D. Škapin from Jožef Stefan Institute, Slovenia, for determination of SSA and SEM measurement of HAp powder, respectively, Dr. I. Castvan and Dr. Dj. Veljovic from Faculty of Technology and Metallurgy, University of Belgrade, Serbia, for determination of SSA of LFP powder and SEM microstructural measurements of sintered ceramics, respectively, and to Dr. Vuk Spasojevic, Vinča Institute for Nuclear Sciences for determination of carbonate content.

**Authors' contributions**

M. J. L. conceived the paper idea, synthesized HAp material, performed particle size distribution measurements, thermal analysis with mass spectrometry and sintering experiments, and wrote the paper. M. K. synthesized LFP powder and was involved in thermal characterization. M. S. performed ion-milling and microstructural characterization of sintered ceramics, while F. B. measured chemical composition and mapping of elemental distributions. L. V. performed XRD measurements on synthesized powders and sintered ceramics, Rietveld analysis, as well as corresponding calculations, and wrote parts of the manuscript related to phase analysis. A.E. measured mechanical properties of the sintered ceramics. All authors contributed to the analysis of results, interpretations, and discussions, as well as paper writing at specific segments. The authors declare no financial and intellectual conflict of interests.

**References**

[1] L.L. Hench, Bioceramics, J. Am. Ceram. Soc. 81 (1998) 1705–1728. doi:10.1111/j.1151-2916.1998.tb02540.x.

[2] O. Korostynska, A.A. Gandhi, A. Mason, A. Al-Shamma'a, S.A.M. Tofail, Biomedical Sensing with Hydroxyapatite Ceramics in GHz Frequency Range, Key Eng. Mater. 543 (2013) 26–29. doi:10.4028/www.scientific.net/KEM.543.26.

[3] H.-C. Wu, T.-W. Wang, M.C. Bohn, F.-H. Lin, M. Spector, Novel Magnetic Hydroxyapatite Nanoparticles as Non-Viral Vectors for the Glial Cell Line-Derived Neurotrophic Factor Gene, Adv. Funct. Mater. 20 (2010) 67–77. doi:10.1002/adfm.200901108.

[4] H. Sun, F.-Z. Su, J. Ni, Y. Cao, H.-Y. He, K.-N. Fan, Gold Supported on Hydroxyapatite as a Versatile Multifunctional Catalyst for the Direct Tandem Synthesis of Imines and Oximes, Angew. Chem. Int. Ed. 48 (2009) 4390–4393. doi:10.1002/anie.200900802.

[5] J. Wang, L.L. Shaw, Nanocrystalline hydroxyapatite with simultaneous enhancements in hardness and toughness, Biomaterials. 30 (2009) 6565–6572. doi:10.1016/j.biomaterials.2009.08.048.

[6] S. Bose, S. Dasgupta, S. Tarafder, A. Bandyopadhyay, Microwave-processed nanocrystalline hydroxyapatite: Simultaneous enhancement of mechanical and biological properties, Acta Biomater. 6 (2010) 3782–3790. doi:10.1016/j.actbio.2010.03.016.
[7] M. Eriksson, Y. Liu, J. Hu, L. Gao, M. Nygren, Z. Shen, Transparent hydroxyapatite ceramics with nanograin structure prepared by high pressure spark plasma sintering at the minimized sintering temperature, J. Eur. Ceram. Soc. 31 (2011) 1533–1540.
[8] M.J. Lukić, Č. Jovalekić, S. Marković, D. Uskoković, Enhanced high-temperature electrical response of hydroxyapatite upon grain size refinement, Mater. Res. Bull. 61 (2015) 534–538. doi:10.1016/j.materresbull.2014.10.072.
[9] K.-H. Zuo, Y.-P. Zeng, D. Jiang, Synthesis and Magnetic Property of Iron Ions-Doped Hydroxyapatite, J. Nanosci. Nanotechnol. 12 (2012) 7096–7100. doi:10.1166/jnn.2012.6578.
[10] R. K, P.K. Mallik, B. Basu, Twinning induced enhancement of fracture toughness in ultrafine grained Hydroxyapatite–Calcium Titanate composites, J. Eur. Ceram. Soc. 36 (2016) 805–815. doi:10.1016/j.jeurceramsoc.2015.10.044.
[11] E. Champion, Sintering of calcium phosphate bioceramics, Acta Biomater. 9 (2013) 5855–5875. doi:10.1016/j.actbio.2012.11.029.
[12] M.A. Fanovich, M.S. Castro, J.M.P. Lopez, Improvement of the microstructure and microhardness of hydroxyapatite ceramics by addition of lithium, Mater. Lett. 33 (1998) 269–272.
[13] T. Goto, N. Wakamatsu, H. Kamemizu, M. Iijima, Y. Doi, Y. Moriwaki, Sintering mechanism of hydroxyapatite by addition of lithium phosphate, J. Mater. Sci. Mater. Med. 2 (1991) 149–152. doi:10.1007/BF00692973.
[14] E.B. Ansar, M. Ajeesh, Y. Yokogawa, W. Wunderlich, H. Varma, Synthesis and Characterization of Iron Oxide Embedded Hydroxyapatite Bioceramics, J. Am. Ceram. Soc. 95 (2012) 2695–2699. doi:10.1111/j.1551-2916.2011.05033.x.
[15] Q. Chang, C.P. Zhang, H.Q. Ru, J.L. Yang, D.L. Chen, Hydroxyapatite reinforced with Ti–Fe particle: correlation between composition, microstructure and mechanical properties, Adv. Appl. Ceram. 113 (2013) 108–113. doi:10.1179/1743676113Y.0000000123.
[16] M. Gauthier, C. Michot, N. Ravet, M. Duchesneau, J. Dufour, G. Liang, J. Wontcheu, L. Gauthier, D.D. MacNeil, Melt Casting LiFePO4 I. Synthesis and Characterization, J. Electrochem. Soc. 157 (2010) A453–A462. doi:10.1149/1.3284505.
[17] M.J. Lukić, L. Veselinović, Z. Stojanović, M. Maček-Kržmanc, I. Bračko, S.D. Škapin, S. Marković, D. Uskoković, Peculiarities in sintering behavior of Ca-deficient hydroxyapatite nanopowders, Mater. Lett. 68 (2012) 331–335. doi:10.1016/j.matlet.2011.10.085.
[18] M.J. Lukić, S.D. Škapin, S. Marković, D. Uskoković, Processing Route to Fully Dense Nanostructured HAp Bioceramics: From Powder Synthesis to Sintering, J. Am. Ceram. Soc. 95 (2012) 3394–3402. doi:10.1111/j.1551-2916.2012.05376.x.
[19] M.J. Lukić, L. Veselinović, M. Stevanović, J. Nunić, G. Dražič, S. Marković, D. Uskoković, Hydroxyapatite nanopowders prepared in the presence of zirconium ions, Mater. Lett. 122 (2014) 296–300. doi:10.1016/j.matlet.2014.02.072.
[20] J. Rodríguez-Carvajal, FullProf2k. Version 2.40-May 2005-LLB JRC, Laboratoire Léon Brillouin (CEA–CNRS), CEA–Sarclay, France, 2005.
[21] L.B. McCusker, R.B. Von Dreele, D.E. Cox, D. Louër, P. Scardi, Rietveld refinement guidelines, J. Appl. Crystallogr. 32 (1999) 36–50. doi:10.1107/S0021889898009856.
[22] R.A. Young, ed., The Rietveld Method, Oxford University Press, Oxford, New York, 1995.
[23] T. Roisnel, J. Rodríquez-Carvajal, WinPLOTR: A Windows Tool for Powder Diffraction Pattern Analysis, Mater. Sci. Forum. 378–381 (2001) 118–123. doi:10.4028/www.scientific.net/MSF.378-381.118.
[24] R.G. Garvey, LSUCRI, least squares unit-cell refinement with indexing on the personal computer, Powder Diffr. 1 (1986) 114.
[25] L.M. Rodríguez-Lorenzo, J.N. Hart, K.A. Gross, Structural and Chemical Analysis of Well-Crystallized Hydroxyfluorapatites, J. Phys. Chem. B. 107 (2003) 8316–8320. doi:10.1021/jp027556o.

[26] J. Rodríguez-Carvajal, Recent advances in magnetic structure determination by neutron powder diffraction, Phys. B Condens. Matter. 192 (1993) 55–69. doi:10.1016/0921-4526(93)90108-I.
[27] P.W. Stephens, Phenomenological model of anisotropic peak broadening in powder diffraction, J. Appl. Crystallogr. 32 (1999) 281–289. doi:10.1107/S0021889898006001.
[28] B. Antic, A. Kremenović, A.S. Nikolic, M. Stoiljkovic, Cation Distribution and Size-Strain Microstructure Analysis in Ultrafine Zn−Mn Ferrites Obtained from Acetylacetonato Complexes, J. Phys. Chem. B. 108 (2004) 12646–12651. doi:10.1021/jp036214v.
[29] A.G. Evans, E.A. Charles, Fracture Toughness Determinations by Indentation, J. Am. Ceram. Soc. 59 (1976) 371–372. doi:10.1111/j.1151-2916.1976.tb10991.x.
[30] E. Landi, A. Tampieri, G. Celotti, S. Sprio, Densification behaviour and mechanisms of synthetic hydroxyapatites, J. Eur. Ceram. Soc. 20 (2000) 2377–2387. doi:10.1016/S0955-2219(00)00154-0.
[31] A. Ait Salah, P. Jozwiak, K. Zaghib, J. Garbarczyk, F. Gendron, A. Mauger, C.M. Julien, FTIR features of lithium-iron phosphates as electrode materials for rechargeable lithium batteries, Spectrochim. Acta. A. Mol. Biomol. Spectrosc. 65 (2006) 1007–1013. doi:10.1016/j.saa.2006.01.019.
[32] I. Belharouak, C. Johnson, K. Amine, Synthesis and electrochemical analysis of vapor-deposited carbon-coated LiFePO4, Electrochem. Commun. 7 (2005) 983–988. doi:10.1016/j.elecom.2005.06.019.
[33] Y.Z. Dong, Y.M. Zhao, P. Fu, H. Zhou, X.M. Hou, Phase relations of Li2O–FeO–B2O3 ternary system and electrochemical properties of LiFeBO3 compound, J. Alloys Compd. 1–2 (2008) 585–590. doi:10.1016/j.jallcom.2007.07.099.
[34] X. Lin, Y. Zhao, Y. Dong, Z. Liang, D. Yan, X. Liu, Q. Kuang, Subsolidus phase relations of Li2O–FeO–P2O5 system and the solid solubility of Li1+xFe1−xPO4 compounds under Ar/H2 atmosphere, J. Mater. Sci. 50 (2015) 203–209. doi:10.1007/s10853-014-8579-3.
[35] P. Valério, F.N. Oktar, G. Göller, L.S. Ozyegin, A.P.M. Shainberg, A. Goes, M.F. Leite, Biocompatibility Evaluation of Lithium-Hydroxyapatite Composites, Key Eng. Mater. 309–311 (2006) 1121–1124. doi:10.4028/www.scientific.net/KEM.309-311.1121.
[36] I. Mobasherpour, M.S. Heshajin, A. Kazemzadeh, M. Zakeri, Synthesis of nanocrystalline hydroxyapatite by using precipitation method, J. Alloys Compd. 430 (2007) 330–333. doi:10.1016/j.jallcom.2006.05.018.
[37] M. Voltolini, H.-R. Wenk, J. Gomez Barreiro, S.C. Agarwal, Hydroxylapatite lattice preferred orientation in bone: a study of macaque, human and bovine samples, J. Appl. Crystallogr. 44 (2011) 928–934. doi:10.1107/S0021889811024344.
[38] A.M. Sofronia, R. Baies, E.M. Anghel, C.A. Marinescu, S. Tanasescu, Thermal and structural characterization of synthetic and natural nanocrystalline hydroxyapatite, Mater. Sci. Eng. C. 43 (2014) 153–163. doi:10.1016/j.msec.2014.07.023.
[39] A.A. White, I.A. Kinloch, A.H. Windle, S.M. Best, Optimization of the sintering atmosphere for high-density hydroxyapatite–carbon nanotube composites, J. R. Soc. Interface. 7 (2010) S529–S539. doi:10.1098/rsif.2010.0117.focus.
[40] J.-P. Lafon, E. Champion, D. Bernache-Assollant, R. Gibert, A.-M. Danna, Termal decomposition of carbonated calcium phosphate apatites, J. Therm. Anal. Calorim. 72 (2003) 1127–1134.
[41] M.A. Fanovich, J.M. Porto López, Influence of temperature and additives on the microstructure and sintering behaviour of hydroxyapatites with different Ca/P ratios, J. Mater. Sci. Mater. Med. 9 (1998) 53–60. doi:10.1023/A:1008834712212.
[42] R.D. Shannon, Revised effective ionic radii and systematic studies of interatomic distances in halides and chalcogenides, Acta Crystallogr. A. 32 (1976) 751–767. doi:10.1107/S0567739476001551.
[43] K. Zhu, K. Yanagisawa, R. Shimanouchi, A. Onda, K. Kajiyoshi, Preferential occupancy of metal ions in the hydroxyapatite solid solutions synthesized by hydrothermal method, J. Eur. Ceram. Soc. 26 (2006) 509–513. doi:10.1016/j.jeurceramsoc.2005.07.019.
[44] T.J. White, Z.L. Dong, Structural derivation and crystal chemistry of apatites, Acta Crystallogr. B. 59 (2003) 1–16. doi:10.1107/S0108768102019894.

[45] H.R. Low, N. Phonthammachai, A. Maignan, G.A. Stewart, T.J. Bastow, L.L. Ma, T.J. White, The Crystal Chemistry of Ferric Oxyhydroxyapatite, Inorg. Chem. 47 (2008) 11774–11782. doi:10.1021/ic801491t.
[46] T. Baikie, G.M.H. Ng, S. Madhavi, S.S. Pramana, K. Blake, M. Elcombe, T.J. White, The crystal chemistry of the alkaline-earth apatitesA10(PO4)6CuxOy(H)z (A = Ca, Sr and Ba), Dalton Trans. (2009) 6722–6726. doi:10.1039/B906639J.
[47] P.E. Kazin, O.R. Gazizova, A.S. Karpov, M. Jansen, Y.D. Tretyakov, Incorporation of 3d-metal ions in the hexagonal channels of the Sr5(PO4)3OH apatite, Solid State Sci. 9 (2007) 82–87. doi:10.1016/j.solidstatesciences.2006.11.005.
[48] N. Song, Y. Liu, Y. Zhang, Y.N. Tan, L.M. Grover, Synthesis and characterisation of iron substituted apatite, (2013). http://www.maneyonline.com/doi/abs/10.1179/1743676112Y.0000000034?token=004811d3367232d45232b4524316a43576b412148743568293c6c567e504f58762f46e1b& (accessed January 8, 2014).
[49] J.R. Ramya, K.T. Arul, K. Elayaraja, S.N. Kalkura, Physicochemical and biological properties of iron and zinc ions co-doped nanocrystalline hydroxyapatite, synthesized by ultrasonication, Ceram. Int. 40 (2014) 16707–16717. doi:10.1016/j.ceramint.2014.08.035.
[50] M.E. Zilm, M. Staruch, M. Jain, M. Wei, An intrinsically magnetic biomaterial with tunable magnetic properties, J. Mater. Chem. B. 2 (2014) 7176–7185. doi:10.1039/C4TB00925H.

## Supporting info

### Specific surface area (SSA) and carbonate content determinations

SSA determination of HAp powder was performed by standard BET method, measuring isothermal adsorption-desorption characteristics of $N_2$ adsorbate**,** at -198.5 °C. Prior to measurement, degassing of sample was performed. Measurements were done on Micromeritics Gemini 2370 V5 device (Norcross, GA, USA). SSA determination of LFP powder was done by the same method, using a Micromeritics ASAP 2020 instrument. Sample was degassed at 110 °C for 10 h under reduced pressure. The specific surface area of samples was from the linear part of the nitrogen adsorption isotherms.

Determination of content of total carbon was performed on LECO elemental analyzer model 628. Instrument range for carbon content is from 0.02 up to 175 mg, and precision range is 0.01 mg. Helium (99,995 %) was used as a carrier gas, whilst the sample was combusted in stream of pure oxygen (99,995 %). Prior to each measurement, calibration check was verified with certified reference material of EDTA.

**Crystallographic parameters, particle size analysis, and phase composition after sintering**

Table SI. Properties of prepared materials.

| Sample | d (*hkl*) / nm | *a* / Å | *b* / Å | *c* / Å | *V* / Å$^3$ | $d_{50}$ – vol.* / µm | $d_{50}$ – num.* / µm |
|---|---|---|---|---|---|---|---|
| HAp | 8.1(*002*) | 9.42665(5) | 9.42665(5) | 6.8816(3) | 529.54(9) | 5.8 | 0.41 |
| LFP | 37 (*311*) | 10.3237(3) | 5.9975(3) | 4.690(5) | 296.76(4) | 10.2 | 0.24 |

*vol. – PSD by volume; num. – PSD by number; $d_{50}$ – average particle size;

Table SII. Phase composition of non-isothermally sintered HAp –LFP composites.

| **Sample** | **Final phase composition$_{XRD}$ / %** | | | |
|---|---|---|---|---|
| | **HAp** | **β-TCP** | **α-TCP** | **Fe- inclusions** |
| HAp | 92.5 | - | 7.5 | - |
| HAp + 1 % LFP | 87 | 13 | - | - |
| HAp + 2 % LFP | 84 | 16 | - | - |
| HAp + 5 % LFP | 74 | 26 | - | - |
| HAp + 10 % LFP | 24 | 76 | - | + |

**Sintering of HAp in air atmosphere**

XRD patterns of HAp powder after high-temperature treatments in air atmosphere are shown. Heating of HAp powder up to 900 °C, which is the temperature where phase transformation and β-TCP formation would already happen in the case of non-stoichiometric, Ca-deficient HAp, did not result in the observable amount of another phase besides HAp. Moreover, application of high-temperature two-step sintering cycle, with the first temperature even at 1250 °C, also showed the exceptional thermal stability of synthesized HAp powder in an air atmosphere. Having in mind these findings, it is clear

that the appearance of α-TCP phase after non-isothermal heating of HAp up to 1200 °C in Ar atmosphere was provoked by the shifted chemical equilibrium of dehydroxylation reaction in the absence of water in the sintering atmosphere.

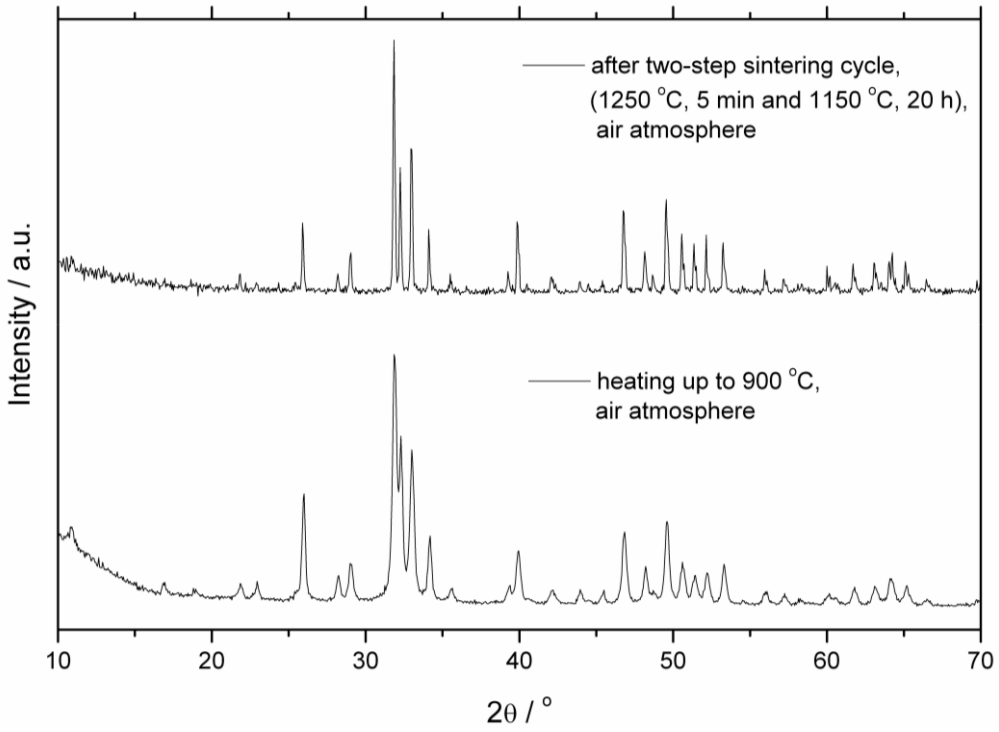


Fig. S1 XRD patterns of HAp powder after different high-temperature treatments.

**Figure captions**

Fig. 1. (a) XRD patterns and PSDs of (b) HAp and (c) LFP powders. (2-column fitting image)

Fig. 2. SEM images of (a) HAp and (b) LFP powders (2-column fitting image)

Fig. 3. FTIR spectra of HAp and LFP powders, and HAp and HAp + 5 % LFP samples after non-isothermal sintering. (single column fitting image)

Fig. 4. TG-DTA and mass spectra of prepared LFP in air, (a) and (b), and in inert (Ar) atmosphere, (c) and (d). (2-column fitting image)

Fig. 5. TG-DTA and mass spectra of HAp, (a) and (b), and HAp + 5 % LFP, (c) and (d), in inert (Ar) atmosphere. (2-column fitting image)

Fig. 6. (a) Non-isothermal densification and (b) densification rate of HAp with different amount of LFP up to 1200 °C in inert (Ar) atmosphere. (2-column fitting image)

Fig. 7. Shrinkage curves with corresponding mass spectra of (a) HAp and (b) HAp +5 % LFP in inert (Ar) atmosphere. (single column fitting image)

Fig. 8. SEM micrographs of microstructural profile of non-isothermally sintered ceramics with different amount of added LFP. (2-column fitting image)

Fig. 9. (a) SEM micrograph of laminar and flat regions of HAp +5 % LFP sample with elemental distribution; (b) SEM micrograph of magnified flat region with clearly observable spherical inclusions with elemental mapping showing Fe-rich region; EDS spectra of (c) laminar and flat regions and (d) Fe-rich inclusions. (2-column fitting image)

Fig. 10. XRD patterns of non-isothermally sintered ceramics up to 1200 °C. (single column fitting image)

Fig. 11. Final Rietveld refined plots of (a) HAp and (b) HAp + 5 % LFP samples after non-isothermal sintering. (single column fitting image)

Fig. 12. (a) Crystallite shape and (b) microstructural strain of HAp and HAp + 5 % LFP samples after non-isothermal sintering. (2-column fitting image)

Fig. 13. (a) Vickers hardness and (b) fracture toughness properties of final ceramics upon non-isothermal sintering (2-column fitting image).

Fig. S1 XRD patterns of HAp powder after different high-temperature treatments.

**Table captions**

Table I. Atomic composition of characteristic microstructural regions.

Table II. The refined values of unit-cell parameters and cell volume.

Table III. The agreement factors, structural and microstructural parameters after non-isothermal sintering.

Table SI. Properties of prepared materials.

Table SII. Phase composition of non-isothermally sintered HAp –LFP composites.